Research Square

Preprints are preliminary reports that have not undergone peer review.
They should not be considered conclusive, used to inform clinical practice,
or referenced by the media as validated information.

Mechanistic insights into target searching, de-dimerization, and activation of Mucilaginibacter paludis Argonaute

wenqiang li

li-wenqiang@hubu.edu.cn

Hubei university https://orcid.org/0000-0002-3951-6691

Chendi Zhang

Hubei university

Yangyang Hu

Hubei university

Jingjing Zhang

Hubei university

Fajun Lai

Hubei university

Zhuang Li

Hubei University https://orcid.org/0000-0002-7249-9029

Lixin Ma

Hubei University https://orcid.org/0000-0002-2016-9781

Article

Keywords:

Posted Date: March 13th, 2026

DOI: https://doi.org/10.21203/rs.3.rs-8986093/v1

License: This work is licensed under a Creative Commons Attribution 4.0 International License.
Read Full License

Additional Declarations: There is **NO** Competing Interest.

Mechanistic insights into target searching, de-dimerization, and activation of *Mucilaginibacter paludis* Argonaute

Author Information

Wenqiang Li[1], Chendi Zhang[1], Yangyang Hu[1], Jingjing Zhang[1], Fajun Lai[1], Zhuang Li[1*], Lixin Ma[1*]

1 State Key Laboratory of Biocatalysis and Enzyme Engineering, Hubei Key Laboratory of Industrial Biotechnology, School of Life Sciences, Hubei University, Wuhan, Hubei 430062, China.

*Corresponding author

Correspondence to: malixing@hubu.edu.cn; zhuangli@hubu.edu.cn;

Abstract

Argonaute proteins are found in both eukaryotes and prokaryotes, participating in defense and gene regulation. Although extensive structural studies have elucidated guide loading, target recognition and catalytic mechanisms of long prokaryotic Argonautes (pAgos), the structural basis underlying target searching remains largely unexplored. Here, we report cryo-electron microscopy structures of the RNA-preferring MbpAgo from *Mucilaginibacter paludis* in guide-bound (3.2 Å) and guide–target-bound (3.1 Å) states. Unexpectedly, guide loading promotes the formation of a symmetric dimer that sandwiches an additional nucleic acid fragment at the dimer interface, revealing a surveillance configuration for candidate target sampling. Progressive guide-target duplex propagation beyond ~12 bp induces pronounced conformational rearrangements, including PAZ domain rotation and inversion of an interlocked PIWI loop, thereby disrupting the dimer interface and generating of a catalytically competent monomer. Stabilization of the dimer through engineered disulfide bonds suppresses cleavage activity, demonstrating that target-triggered de-dimerization is required for activation. Together, our findings uncover a structural framework for target searching in an RNA-preferring pAgo and uncover a monomer-dimer-monomer activation

trajectory in which guide-induced dimerization is followed by target-triggered de-dimerization, establishing assembly-state remodeling as a regulatory principle in pAgo-mediated nucleic acid recognition.

Introduction

Argonaute proteins (Agos) function as DNA- or RNA-guided endonucleases with high specificity for target recognition and cleavage across all domains of life[1-4]. Eukaryotic Argonaute proteins (eAgos) employ small RNA guides to target complementary RNA molecules, playing central roles in gene silencing pathways and antiviral defense[5, 6]. In contrast, prokaryotic Argonaute proteins (pAgos) perform analogous defense functions against invading genetic elements and also participate in diverse cellular processes, including DNA replication, processing, and repair[3, 7-10]. Phylogenetically, pAgos are classified into three major clades: active long-A, inactive long-B, and short pAgos[3, 9, 11]. Similar to eAgos, long pAgos share a conserved bilobed architecture, with the N-terminal lobe consisting of the N, L1 (Linker 1), and PAZ (Piwi-Argonaute-Zwille) domains, connected via interdomain linker L2 to the C-terminal lobe consisting of the MID (Middle) and PIWI (P-element induced wimpy testis) domains[3, 9]. The guide-target duplex is accommodated within a central channel formed between the two lobes, allowing for precise positioning of the nucleic acids for sequence-specific recognition and cleavage. The MID and PAZ domains anchor the 5' and 3' ends of the guide strand, respectively, while the PIWI domain adopts an RNase H-like fold and harbors a conserved catalytic tetrad (DEDX motif, where X is D, H, or K) that coordinates two divalent metal cations essential for target cleavage[3]. long-B pAgos carry substitutions in the catalytic tetrad, rendering them inactive as endonucleases. Short pAgos, which lack the PAZ and N domains, retain only the MID and a catalytically inactive PIWI domain[12]. However, they typically associate with effector proteins that contain an APAZ (analog of PAZ) domain and other divergent enzymatic domains, which compensate for the loss of PIWI-mediated cleavage activity.

Owing to their relatively small protein size and the lack of strong requirements for specific motifs during guide binding or target recognition, pAgos have the potential as versatile tools for nucleic acid manipulation and genomic technologies[13-16]. Most characterized long-A pAgos utilize small DNA guides

to cleave DNA targets, while a distinct subgroup of CRISPR-associated pAgos employs small RNA guides to act on DNA[17-21]. Although several DNA-targeting pAgos have also been shown to cleave RNA *in vitro*, their RNA cleavage activity is typically lower than for DNA[20, 22-24]. A smaller subset of pAgos has been identified that uses DNA guides with a strong preference for RNA targets[17, 25, 26], functionally resembling eAgos in their substrate choice. Extensive biochemical and structural studies have been conducted to elucidate the mechanism for guide and target recognition, as well as activation of long pAgos. Typically, the guide nucleotides 2 to 8, counted from the 5'-end of the guide strand, constitute the seed segment, which is pre-organized in a helical conformation and exposed to the solvent[24, 27, 28]. Base pairing of the seed segment with the target initiates conformational changes that promote the propagation of guide–target duplex[24]. Upon target engagement, the N and PAZ domains undergo pivot-like conformational rearrangements, leading to the release of the 3' end of the guide via a rotation of the PAZ domain[24, 29-32]. Importantly, further propagation of the guide–target duplex induces structural transitions within the nucleic acid-binding surface of the PIWI domain, particularly involving dynamic movements in loops L1 and L2[33]. A key catalytic event occurs when the glutamic acid residue from loop L2 (termed the Glu finger) inserts into the active site, enabling the cleavage of the target strand between the nucleotides paired with guide positions 10 and 11[33-36].

Previous insights into the mechanisms of guide and target recognition and activation in long pAgos were mainly derived from X-ray crystallography studies[3, 17, 20, 34, 37, 38]. Recent studies have revealed that higher-order assembly can modulate pAgo activity. Cryo-electron microscopy (cryo-EM) analysis of the thermophilic archaeal PfAgo from *Pyrococcus furiosus* in our earlier work uncovered target-induced dimerization that stabilizes catalytic loops and enhances activity[35]. Similar assembly-dependent regulation has been observed in the mesophilic CpAgo from *Clostridium perfringens* and short pAgos[29, 39-44], suggesting that transitions in oligomeric state may represent a conserved regulatory strategy. Nevertheless, how assembly-state transitions contribute to target searching and activation remains unclear.

Here, we investigate MbpAgo from the psychrotolerant bacterium *Mucilaginibacter paludis*, the first characterized pAgo that preferentially cleaves RNA using DNA guides. Cryo-EM structures of MbpAgo in

guide-bound and guide–target-bound states, combined with biochemical and mutagenesis analyses, reveal an unexpected assembly transition mechanism. MbpAgo forms a dimeric guide-bound complex compatible with target scanning. Initial target engagement disrupts the dimer interface, and subsequent duplex propagation stabilizes a monomeric, catalytically competent conformation. These findings uncover an assembly-state remodeling mechanism that links target searching to activation in an RNA-preferring prokaryotic Argonaute.

Results

Structure of the MbpAgo guide-bound binary complex reveals a dimeric scanning configuration

Our previous biochemical characterization indicated that a 16-nt guide DNA is optimal for MbpAgo-mediated cleavage activity[25]. To elucidate the structural basis for target recognition and cleavage, we first assembled the MbpAgo-guide DNA binary complex by incubating the wild-type MbpAgo with a 16-nt 5'-phosphorylated guide DNA (5'P-TGAGGTAGTAGGTTGT), and determined the cryo-EM structure of this complex at 3.2 Å resolution (Fig. 1 and Supplementary Fig. 1). Most of the amino acids and nucleotides can be modelled except for several flexible loops (residues 24-35, 231-239, 511-518 and 593-600 in one molecular, residues 12-110, 185-204, 218-284 and 593-601 in the other). Similar to previously reported Ago structures[3], MbpAgo adopts the canonical bilobed architecture composed of the N domain (1–100), interdomain linker L1 (100–180), PAZ domain (181–305), and interdomain linker L2 (306–385), MID domain (386–548), and PIWI domain (549–795). Unexpectedly, the binary complex adopts a symmetric dimeric architecture, with excess DNA density positioned between the two MbpAgo molecules (Fig. 1C).

Similarly to previously studied Ago proteins[3, 18, 20, 30, 35, 37], the 5' and 3' terminal nucleotides of the gDNA are anchored in the MID and PAZ domains of MbpAgo, respectively (Fig. 1C). The first base is flipped out and stacked with the side chain of His^{482}, and the 5'-phosphate is anchored in a highly conserved amino-acid motif in the MID domain with His^{482}, Lys^{486}, and Gln^{495} residues (Supplementary Fig. 2A). Moreover, the 5'-phosphate is juxtaposed to the 3rd phosphate, and a metal ion coordinated by the Gln^{496} and Glu^{541} stabilizes these phosphates (Supplementary Fig. 2A). Our previous studies have found that

divalent metal ions are important for MbpAgo to bind the 5'P group of the guide, and mutations in this motif impair guide DNA binding and precise cleavage of the target[25]. MbpAgo has no further contact with the first nucleobase, explaining why MbpAgo did not show a significant preference for guides with a particular 5' nucleotide. The gDNA is enclosed by L1, L2 and PIWI domains, capped by the MID domain on one end and PAZ domain on the other end, and extensively coordinated within MbpAgo through multiple contacts between the DNA backbone and positively charged amino acid residues (Supplementary Fig. 2B). These interactions pre-organize the guide into a near A-form conformation from nucleotides 1–6 making it suitable for target recognition (Supplementary Fig. 2C). Notably, the excess DNA bases situated between two MbpAgo molecules could serve as candidate target strands and probed by the exposed seed segment of the guide through base-pairing.

MbpAgo dimerization is mediated by cooperative protein–protein and protein–DNA interactions

The dimeric structure reveals two binary complex units arranged face-to-face, stabilizing the structure through interactions at five distinct patches, including two L2-L2 interfaces, one N-PIWI-PIWI-N interface, and two L2-MID-L1-PAZ interfaces (Fig. 2). Unlike the dimerization mode observed in some pAgos mediated solely by specific protein-protein interactions, dimerization of MbpAgo is reinforced by both specific protein-protein interactions and protein-candidate target interactions. The interface contains extensive polar and hydrophobic contacts (Fig. 2A). At L2-L2 interface, R369 forms salt bridge with E312' (' denotes the amino acid from the other molecule) (Fig. 2B). An inter-locked loop (684-690) contributes critically to PIWI-PIWI interface, where Y688 insert into a hydrophobic pocket formed by F364', V695', and Y714', and also forms cation-pi interaction with K2' (Fig. 2B). At L2-MID-L1-PAZ interface, Y373 and Y301' stack with the nucleobase of candidate target DNA, and R530 forms salt bridges with the nucleobase (Fig. 2C and Supplementary Fig. 2C). Together, these amino acids form a unique pocket that captures one end of the candidate target, and due to the dimerization of MbpAgo, an equivalent pocket binds the opposite end (Supplementary Fig. 2C).

To determine the functional state of MbpAgo, we created grouped mutations at the dimer interface and confirmed using AlphaFold3[45] that these mutations did not disrupt the overall protein fold. Group-1 alanine

substitutions (Y301A, Y373A, R530A), group-2 substitutions (R369A, E312A, Y688A, F364A, V695A, Y714A, K2A), and group-3 replacement of the PIWI-loop (684–690) with glycines all impaired dimerization, but did not significantly affect preference for target or cleavage activity (Fig. 2D, E and Supplementary Fig. 3A, B). Similarly, these mutations had no detectable effect on guide-binding affinity (Supplementary Fig. 3C). Based on subsequent structural and biochemical analyses of the ternary complex, MbpAgo is catalytically active as a monomer, explaining why disruption of dimerization does not impair cleavage. These findings indicate that MbpAgo is catalytically active as a monomer and suggest that dimerization primarily facilitates early target engagement rather than catalysis, particularly seed-region interrogation. Consistently, binding assays using a short seed-complementary targets revealed a substantial reduction in binding affinity for group-1 mutations at the protein–DNA interface, supporting a role for the dimer in candidate target capture (Supplementary Fig. 3D).

Target binding induces dimer disruption and stabilizes a monomeric catalytic state

Next, we assembled the ternary complex by incubating the wild-type MbpAgo with 16 nt guide DNA and 18 nt target DNA (TACAACCTACTACCTCAT), and determined the structure of this complex at 3.1 Å (Fig. 3A and Supplementary Fig. 4). Most of the amino acids and nucleotides can be modelled, except for several flexible loops (residues 20-107, 189-196, 224-263, 270-276, 511-520 and 595-604). In contrast to the binary complex, the ternary complex is monomeric and accommodates a continuous 15-bp guide–target duplex spanning guide positions 2–16 (Fig. 3A). Although the 5’ nucleotides of the guide remain anchored in the MID domain, target binding drives release of 3’ end of the guide from the PAZ pocket, enabling formation of a 15-bp duplex spanning guide positions 2–16 (Fig. 3B). Substantial structural changes accompany the transition from the binary to the ternary state (Fig. 3C). These include a pronounced rotation of the PAZ domain and repositioning of L1 loops across the PIWI surface that interfaces with nucleic acids. Notably, the interlocked PIWI-loop (residues 684–690), critical for maintaining the PIWI–PIWI interactions in the binary-state dimer, undergoes a flipping motion (Fig. 3C). This reorientation displaces Y688, disrupting the hydrophobic and cation–π interactions essential for dimer stabilization. Together, these changes promote a dimer-to-monomer transition. Moreover, superposition analysis reveals severe

steric clashes if two ternary protomers are forced into the binary dimer configuration, indicating that duplex propagation is incompatible with the dimeric state (Figure 4D). These observations strongly suggest that MbpAgo must disengage from its dimeric form and adopt a monomeric conformation to become catalytically competent—consistent with our earlier finding that dimer-disrupting mutations do not impair cleavage. To experimentally test whether monomerization is required for activity, we engineered an N686C mutant to lock the dimer via intermolecular disulfide bond formation. The covalently linked dimer displayed markedly reduced cleavage activity, which was restored upon reduction with DTT (Figure 4E-G), confirming that the monomeric state is catalytically competent. Together, these results highlight the crucial role of the dimer-to-monomer transition in MbpAgo activation.

Duplex length and complementarity dictate the dimer-to-monomer transition

In a previous study on PfAgo, propagation of the guide–target duplex drives a monomer-to-dimer transition that activates target cleavage[35]. In contrast, our results reveal that MbpAgo undergoes the opposite process: target engagement induces a dimer-to-monomer transition that is essential for its catalytic activation. To determine the minimal target length capable of triggering MbpAgo de-dimerization, we assembled a series of ternary complexes containing the 16-nt guide DNA and target DNAs of varying lengths (7-, 8-, 10-, 11-, 12-, 14-, and 16-bp complementarity), thereby mimicking progressive guide–target duplex propagation. The results showed that seed pairing of 7-8 bp preserved the dimeric state, whereas duplexes $\geqslant$10 bp progressively shifted the equilibrium toward monomer, with nearly complete monomerization observed for $\geqslant$14 bp complementarity (Fig. 4A), indicating that a guide–target duplex of at least 14 bp is required to fully disrupt the dimeric interface and induce MbpAgo de-dimerization. We further evaluated 16-nt targets harboring mismatches of varying lengths at either end and found that targets harboring mismatches failed to trigger monomerization unless >12 perfectly matched base pairs were maintained (Fig. 4B), indicating that both duplex length and fidelity are required for this transition. Given that MbpAgo prefers RNA substrates, we also tested whether RNA targets trigger similar conformational changes. The results indicate that RNA targets induced an equivalent structural switch (Fig. 4C), demonstrating that target-induced de-

dimerization represents a general feature of MbpAgo activation. Ensemble FRET measurements further confirmed a decrease in FRET efficiency upon target addition, consistent with disruption of the dimer and formation of the active monomeric state (Fig. 4D). Together, these findings demonstrate that target-induced de-dimerization is a prerequisite for MbpAgo activation.

Working model of MbpAgo activation

Altogether, these presented data support a working model in which MbpAgo cycles through distinct assembly states during target recognition (Figure 5). Apo MbpAgo exists as a monomer, and guide binding promotes formation of a dimeric scanning complex that captures candidate targets through seed interrogation. Progressive guide–target duplex propagation destabilizes the dimer interface, triggering a dimer-to-monomer transition that licenses catalytic activation. MbpAgo therefore undergoes a characteristic "monomer → dimer → monomer" assembly transition, coupling target searching to nuclease activation.

Discussion

Structural and biochemical studies have established that most characterized long-A pAgos function as monomers, with guide–target duplex formation directly triggering catalytic activation within the PIWI domain[24, 29, 34, 38]. More recently, alternative regulatory paradigms have emerged. In PfAgo, TtdAgo and CpAgo, target engagement promotes dimerization that stabilizes catalytic loops and enhances cleavage efficiency[29, 35]. These observations have broadened the mechanistic landscape of long-A pAgo regulation beyond simple monomeric activation. In contrast to these systems, MbpAgo follows a fundamentally different regulatory logic. The most striking observation is that guide loading drives the formation of a stable dimeric assembly that captures candidate nucleic acids at the MbpAgo dimer interface. Target engagement disrupts this preformed dimer and converts MbpAgo into a monomeric, catalytically competent state. This reverse activation trajectory—dimer-to-monomer transition upon duplex propagation—distinguishes MbpAgo from the aforementioned long-A pAgos. Whether similar mechanisms operate in other RNA-preferring pAgos remains to be determined.

Oligomerization-dependent regulation appears to be a common theme across diverse prokaryotic Argonaute systems. In several short pAgo-based immune pathways, guide–target duplex formation often induces higher-order assembly that activates associated effector domains. For example, in SPARTA and SPARSA systems, RNA guide and DNA target binding promote Ago dimerization, followed by tetramerization of TIR or Sir2 domains to trigger NAD^+ hydrolysis[39-41, 46]. More recently, short pAgos coupled to nuclease domains, such as SPARDA and SPARHA, have been shown to employ filament-based activation mechanisms[42-44]. Notably, distinct activation trajectories have been observed, ranging from "dimer–monomer–filament" to "monomer–dimer–monomer–filament" transitions[42, 44]. Together with these systems, the monomer–dimer–monomer transition uncovered for MbpAgo, as well as target-induced dimerization in other long pAgos, highlights a common principle: dynamic remodeling of assembly state (monomerization, dimerization, or higher-order oligomerization) serves as a central regulatory strategy to control the activity of pAgo or its interacting proteins.

A particularly unexpected feature of MbpAgo is the presence of an excess nucleic acid fragment captured between the two protomers in the guide-loaded binary complex, which directly contributes to dimer stabilization. MbpAgo dimerization is mediated by defined protein–protein interfaces, including L2–L2, N–PIWI–PIWI–N, and L2–MID–L1–PAZ contacts, with a uniquely interlocked PIWI loop enforcing a symmetric dimer architecture. Two distinct pockets at the L2–MID–L1–PAZ interface further engage the excess nucleic acid together with the guide. We propose that this nucleic acid fragment represents a candidate target transiently sampled through guide seed pairing, revealing a previously unrecognized target-searching mode. In this model, target interrogation is co-mediated by two MbpAgo–gDNA complexes, potentially increasing the target capture efficiency and discrimination. If the two guides differ in sequence, cooperative scanning could further expand the target-search space, providing a flexible and economical strategy for nucleic acid surveillance.

Our systematic analysis of duplex length and base pairing fidelity reveals that MbpAgo activation requires continuous guide–target pairing exceeding ~12 bp. Duplex propagation induces coordinated rotation of the PAZ domain and inversion of the interlocked PIWI loop, destabilizing the dimer interface.

Stabilization of the dimer through engineered intermolecular disulfide bonds markedly suppresses catalytic activity, which can be restored upon bond reduction, establishing that dimer-to-monomer conversion is a prerequisite for activation. These observations suggest that dimerization represents an inactive or surveillance state, analogous to regulatory strategies observed in other bacterial defense proteins[47, 48]. Dimer disassembly releases catalytically competent monomers to execute target cleavage, while freed protomers may reassemble into dimers to resume target searching, reflecting a dynamic and resource-efficient regulatory cycle.

In summary, our study uncovers a previously unrecognized mechanism of target surveillance and activation in MbpAgo, characterized by guide-induced dimerization followed by target-triggered de-dimerization. This reverse regulatory logic sets MbpAgo apart from all previously characterized Argonaute systems and substantially expands the mechanistic repertoire of pAgo-mediated nucleic acid recognition. These findings underscore the remarkable diversity of Argonaute regulatory strategies and provide a conceptual and structural framework for the rational engineering of pAgo-based biotechnological tools.

Methods

Protein Expression and Purification

The plasmids pET28a-MbpAgo and pET28a-MbpAgo_DM (inactive double mutant: D566A, D635A) were constructed by our laboratory in a previous study[25]. All the primers used for constructing mutant in this study are listed in Supplementary Table S2. For protein expression, the strain *Escherichia coli* Rosetta (DE3) (Novagen) was utilized to express MbpAgo and the related mutant proteins. Cultures were grown in the Luria-Bertani (LB) broth supplemented with 50 μg/mL kanamycin at 37°C with aeration until the OD_{600} reached 0.8. The cultures were induced with 0.5 mM IPTG, grown for 16 h at 18 °C, and harvested by centrifugation. The cell pellet was resuspended in Buffer A (20 mM Tris-HCl, pH 7.4, 500 mM NaCl, 20 mM imidazole), supplemented with 10% glycerol and 1 mM PMSF. Then the cells were lysed using a high-pressure homogenizer and centrifuged at 16000 rpm for 45 min. The supernatant was loaded onto Ni-NTA agarose resin with rotation for 1 h. The beads were washed with Buffer A containing 50 mM imidazole and

eluted with Buffer A containing 150 mM imidazole. Fractions containing MbpAgo or mutant were concentrated to a volume of 500 μL using an Amicon 50K filter unit (Millipore). Next, the concentrated proteins were purified on a size exclusion column (Superdex 200 increase 10/300GL, Cytiva) equilibrated with Buffer B (20 mM Tris-HCl, pH 7.4, 150 mM NaCl), and finally stored in Buffer B. Aliquots of 20 μL proteins were flash-frozen in liquid nitrogen and stored at -80 °C.

Assembly of MbpAgo-related complex

Guides and targets were dissolved with assembly Buffer C (20 mM Tris-HCl, pH 7.4, 150 mM NaCl, 5 mM Mg^{2+}). For the assembly of the MbpAgo-gDNA binary complex, MbpAgo protein and 16 nt 5'P-gDNA were incubated at a molar ratio of 1:1.1 in Buffer C at 37°C for 10 min. The MbpAgo-gDNA-target ternary complex was obtained by first mixing MbpAgo protein and 16 nt 5'P-gDNA at a molar ratio of 1:1.1 in Buffer C at 37°C for 10 min. Then the 18 nt target DNA was added into the above mixture at a molar ratio of 1:1.1:1.1 and incubated in Buffer C at 37°C for 30 min. The final volume was 500 μL, and the amount of MbpAgo protein was 2 mg. The acquired MbpAgo complexes were further purified by a size exclusion column (Superdex 200 Increase 10/300 GL, Cytiva) in Buffer C. Finally, fractions containing purified MbpAgo complexes at the peak of the chromatogram were selected for subsequent structural analysis.

Electron microscopy

Aliquots of 4 μL *in vitro* assembled MbpAgo complex samples (0.6 mg/ml) were applied to glow-discharged Quantifoil holey carbon grids (Au, R1.2/1.3, 200 mesh). The grids were blotted with force 2 for 10s and plunged into liquid ethane using a Vitrobot. Cryo-EM data were collected with a Titan Krios microscope (FEI) operated at 300 kV, and images were collected using EPU[49] at a nominal magnification of 105,000x (resulting in a calibrated physical pixel size of 0.85 Å/pixel) with a defocus range from -1.2 μm to -2.2 μm. The images were recorded on a K3 summit electron direct detector in super-resolution mode at the end of a GIF-Quantum energy filter operated with a slit width of 20 eV. A dose rate of 15 electrons per pixel per second and an exposure time of 2.5 s were used, generating 40 movie frames with a total dose

of ~54 electrons per Å. A total of 4,829 and 2,063 movie stacks were collected for MbpAgo-gDNA and MbpAgo-gDNA-tDNA, respectively (Table 1).

Image processing

The movie frames were imported to RELION-3[50], aligned using MotionCor2[51] with bin 2, and subjected to contrast transfer function (CTF) estimation using Gctf[52] on the fly.

For the MbpAgo-gDNA dataset, 2,034,645 particles were picked with a template and extracted from the dose-weighted micrographs. 525,215 particles were selected from 2D classification. 9,000 particles from different views were used to generate initial models in cryoSPARC[53]. 3D classification was performed to distinguish different conformational states. 274,970 particles were used for final 3D refinement with C1 symmetry, converging at 3.2 Å resolution. Details of the cryo-EM image processing are summarized in Table 1.

For the MbpAgo-gDNA-tDNA dataset, 4,017,853 particles were picked with a template and extracted from the dose-weighted micrographs. 1,408,351 particles were selected from 2D classification. 9,000 particles from different views were used to generate initial models in cryoSPARC. 3D classification was performed to distinguish different conformational states. 964,147 particles were used for the final 3D refinement, converging at 3.1 Å resolution. Details of the cryo-EM image processing are summarized in Table 1.

Model building, refinement, and visualization

For high-resolution model building, AlphaFold2-predicted[54] MbpAgo was manually adjusted against the corresponding cryo-EM maps using Coot[55]. Guide DNA and target DNA were built de novo using Coot. Model refinement was performed using Phenix.real_space_refine tool in Phenix[56]. The refinement statistics are summarized in Table 1. Figures were generated via PyMOL and UCSF Chimera.

Single-stranded nucleic acid cleavage activity assay

Cleavage assays were performed using 5'-FAM-labeled targets (45 nt in length) and 5'-P guides (16 nt in length) under conditions described previously study[25] (see Supplementary Table S1 for oligonucleotide sequences). The purified MbpAgo, guides, and targets were mixed with a molar ratio of 4:2:1 (800 nM MbpAgo: 400 nM guide: 200 nM target) in buffer RB (10 mM HEPES-NaOH pH 7.5, 100 mM NaCl, 5% glycerol), supplemented with 5 mM $MnCl_2$. Then the samples were incubated for 30 min at 37 °C for target cleavage. Kinetic analyses of RNA cleavage were performed under single turnover conditions described in the literature, and the data were fitted to the following single exponential equation: $C = Cmax \times [1 – exp(–k_{obs} \times t)]$, where C is the cleavage efficiency at a given time point, Cmax is the maximum cleavage, and k_{obs} is the observed rate constant. All reactions were terminated by adding an equal volume of 2×RNA loading dye (95% formamide, 18 mM EDTA, 0.025% SDS and 0.025% bromophenol blue), followed by heating for 5 min at 95°C. The cleavage products were resolved by 20% denaturing polyacrylamide gel and visualized using Gel Doc™ XR+ (Bio-Rad).

Guide and target binding assays by Fluorescence Polarization

Equilibrium binding of guide and target by MbpAgo or mutants was determined by measuring the changes in fluorescence polarization using SPARK microplate reader (TECAN), equipped with excitation filter of 485/20 nm and emission filter of 535/20. For guide binding assays, MbpAgo and the guide were incubated in buffer RB containing 5 mM Mn^{2+} for 30 min at 25°C in black 96-well half-area plates (Corning). The concentration of the internally FAM-labeled fluorescent guide was fixed at a final 2.5 nM in 100 μL reaction system, whereas the concentration of MbpAgo varied. Following incubation, the samples were read at 535 nm at an excitation of 485 nm. For target binding assays, MbpAgo and label-free guide (1:1) with varying concentrations were incubated for 10 min at 37°C. Subsequently, 2.5 nM 5'-FAM-labeled target was added to the reaction for 1 h at 25°C in buffer RB with 5 mM Mn^{2+}. To determine the apparent dissociation constants (Kd) for guide binding by MbpAgo and target binding by the MbpAgo–gDNA complex, the data were normalized by subtraction of the initial polarization of free fluorescein-labeled guide or target and fitted using the one-site special binding equation, utilizing Prism 9 (GraphPad).

Ensemble fluorescence resonance energy transfer assay

The stopped-flow experiments were performed on an SX20 instrument (Applied Photophysics Inc.) at 25 °C in buffer RB. The 5'-P-labeled and 3'-Cy3/Cy5-labeled guide DNA (gDNA) of 16 nt length were synthesized by Sangon. 200 pmol 3'-Cy3-labeled gDNA were premixed with 200 pmol Cy5-labeled gDNA, then combined with 400 pmol MbpAgo in buffer RB supplemented with 5 mM $MgCl_2$ for 10 min at 25°C for the formation of MbpAgo-gDNA complex (syringe A). Syringe A and syringe B containing 600 pmol 18 nt target DNA were rapidly mixed, and fluorescence data were collected. The final volume of each syringe was 1.5 mL, and the mixing schemes are denoted by cartoon schematics within the figure panels. The samples were excited at 520 nm, and the Cy3 and Cy5 emissions were captured using a 570 nm bandpass filter and a 610 nm long-pass filter, respectively. The FRET traces for the experiments were recorded over 60 s by collecting 2400 time points. All traces were analyzed using Applied Photophysics ProData^{TM} software. All experiments were repeated a minimum of three times, and SEM from the individual fits is noted in the figure legends.

Statistical information

Statistical analyses were performed using GraphPad Prism 9 and Microsoft Excel. The two-tailed Student's t-test was utilized to compare differences between two groups, with significance set at a p-value < 0.05. All data are shown as mean ± standard deviation from three independent replicates.

Data Availability

Cryo-EM reconstructions of MbpAgo-gDNA binary complex and MbpAgo-gDNA-tDNA ternary complex have been deposited in the Electron Microscopy Data Bank under the accession numbers EMD-68672 and EMD-68673, respectively. Coordinates for atomic models of MbpAgo-gDNA binary complex and MbpAgo-gDNA-tDNA ternary complex have been deposited in the Protein Data Bank under the accession numbers 22UE and 22UF, respectively. The online version contains supplementary material.

References

1. Bobadilla Ugarte P, Barendse P, Swarts DC. Argonaute proteins confer immunity in all domains of life. *Curr Opin Microbiol* **74**, 102313 (2023).

2. Swarts DC, *et al.* The evolutionary journey of Argonaute proteins. *Nat Struct Mol Biol* **21**, 743-753 (2014).
3. Lisitskaya L, Aravin AA, Kulbachinskiy A. DNA interference and beyond: structure and functions of prokaryotic Argonaute proteins. *Nat Commun* **9**, 5165 (2018).
4. Olina AV, Kulbachinskiy AV, Aravin AA, Esyunina DM. Argonaute Proteins and Mechanisms of RNA Interference in Eukaryotes and Prokaryotes. *Biochemistry (Mosc)* **83**, 483-497 (2018).
5. Meister G. Argonaute proteins: functional insights and emerging roles. *Nat Rev Genet* **14**, 447-459 (2013).
6. Sheu-Gruttadauria J, MacRae IJ. Structural Foundations of RNA Silencing by Argonaute. *J Mol Biol* **429**, 2619-2639 (2017).
7. Kuzmenko A, *et al.* DNA targeting and interference by a bacterial Argonaute nuclease. *Nature* **587**, 632-637 (2020).
8. Jolly SM, *et al. Thermus thermophilus* Argonaute Functions in the Completion of DNA Replication. *Cell* **182**, 1545-1559 e1518 (2020).
9. Wu J, Yang J, Cho WC, Zheng Y. Argonaute proteins: Structural features, functions and emerging roles. *J Adv Res* **24**, 317-324 (2020).
10. Olovnikov I, Chan K, Sachidanandam R, Newman DK, Aravin AA. Bacterial argonaute samples the transcriptome to identify foreign DNA. *Mol Cell* **51**, 594-605 (2013).
11. Ryazansky S, Kulbachinskiy A, Aravin AA. The Expanded Universe of Prokaryotic Argonaute Proteins. *mBio* **9**, (2018).
12. Prostova M, *et al.* DNA-targeting short Argonautes complex with effector proteins for collateral nuclease activity and bacterial population immunity. *Nat Microbiol* **9**, 1368-1381 (2024).
13. Kropocheva EV, Lisitskaya LA, Agapov AA, Musabirov AA, Kulbachinskiy AV, Esyunina DM. Prokaryotic Argonaute Proteins as a Tool for Biotechnology. *Mol Biol* **56**, 854-873 (2022).
14. Hegge JW, Swarts DC, van der Oost J. Prokaryotic Argonaute proteins: novel genome-editing tools? *Nat Rev Microbiol* **16**, 5-11 (2018).
15. Graver BA, Chakravarty N, Solomon KV. Prokaryotic Argonautes for in vivo biotechnology and molecular diagnostics. *Trends Biotechnol* **42**, 61-73 (2024).
16. Huang S, Wang K, Mayo SL. Genome manipulation by guide-directed Argonaute cleavage. *Nucleic Acids Res* **51**, 4078-4085 (2023).
17. Lisitskaya L, *et al.* Programmable RNA targeting by bacterial Argonaute nucleases with unconventional guide binding and cleavage specificity. *Nat Commun* **13**, 4624 (2022).
18. Lapinaite A, Doudna JA, Cate JHD. Programmable RNA recognition using a CRISPR-associated Argonaute. *Proc Natl Acad Sci U S A* **115**, 3368-3373 (2018).
19. Wang L, *et al.* A bacterial Argonaute with efficient DNA and RNA cleavage activity guided by small DNA and RNA. *Cell Rep* **41**, 111533 (2022).
20. Kaya E, *et al.* A bacterial Argonaute with noncanonical guide RNA specificity. *Proc Natl Acad Sci U S A* **113**, 4057-4062 (2016).
21. Agapov A, Panteleev V, Kropocheva E, Kanevskaya A, Esyunina D, Kulbachinskiy A. Prokaryotic Argonaute nuclease cooperates with co-encoded RNase to acquire guide RNAs and target invader DNA. *Nucleic Acids Res* **52**, 5895-5911 (2024).
22. Kropocheva E, Kuzmenko A, Aravin AA, Esyunina D, Kulbachinskiy A. A programmable pAgo nuclease with universal guide and target specificity from the mesophilic bacterium *Kurthia massiliensis*. *Nucleic Acids Res* **49**, 4054-4065 (2021).
23. Liu Y, *et al.* A programmable omnipotent Argonaute nuclease from mesophilic bacteria *Kurthia massiliensis*. *Nucleic Acids Res* **49**, 1597-1608 (2021).
24. Wang Y, *et al.* Nucleation, propagation and cleavage of target RNAs in Ago silencing complexes. *Nature* **461**, 754-761 (2009).
25. Li W, *et al.* A programmable pAgo nuclease with RNA target preference from the psychrotolerant bacterium *Mucilaginibacter paludis*. *Nucleic Acids Res* **50**, 5226-5238 (2022).

26. Liu Q, *et al.* A programmable pAgo nuclease with RNA target-cleavage specificity from the mesophilic bacterium *Verrucomicrobia*. *Acta Biochim Biophys Sin (Shanghai)* **55**, 1204-1212 (2023).
27. Kuzmenko A, Yudin D, Ryazansky S, Kulbachinskiy A, Aravin AA. Programmable DNA cleavage by Ago nucleases from mesophilic bacteria *Clostridium butyricum* and *Limnothrix rosea*. *Nucleic Acids Res* **47**, 5822-5836 (2019).
28. Parker JS, Parizotto EA, Wang M, Roe SM, Barford D. Enhancement of the seed-target recognition step in RNA silencing by a PIWI/MID domain protein. *Mol Cell* **33**, 204-214 (2009).
29. Liu Y, *et al.* The PAZ pocket and dimerization drive CpAgo's guide-independent and DNA-guided dual catalysis. *Nat Commun* **16**, 6599 (2025).
30. Tao X, *et al.* Structural and mechanistic insights into a mesophilic prokaryotic Argonaute. *Nucleic Acids Res* **52**, 11895-11910 (2024).
31. Wang Y, Juranek S, Li H, Sheng G, Tuschl T, Patel DJ. Structure of an argonaute silencing complex with a seed-containing guide DNA and target RNA duplex. *Nature* **456**, 921-926 (2008).
32. Wang Y, Sheng G, Juranek S, Tuschl T, Patel DJ. Structure of the guide-strand-containing argonaute silencing complex. *Nature* **456**, 209-213 (2008).
33. Sheng G, *et al.* Structure-based cleavage mechanism of *Thermus thermophilus* Argonaute DNA guide strand-mediated DNA target cleavage. *Proc Natl Acad Sci U S A* **111**, 652-657 (2014).
34. Hegge JW, *et al.* DNA-guided DNA cleavage at moderate temperatures by *Clostridium butyricum* Argonaute. *Nucleic Acids Res* **47**, 5809-5821 (2019).
35. Wang L, *et al.* Molecular mechanism for target recognition, dimerization, and activation of *Pyrococcus furiosus* Argonaute. *Mol Cell* **84**, 675-686 e674 (2024).
36. Lei J, *et al.* Two symmetric arginine residues play distinct roles in Thermus thermophilus Argonaute DNA guide strand-mediated DNA target cleavage. *Proc Natl Acad Sci U S A* **116**, 845-853 (2019).
37. Willkomm S, *et al.* Structural and mechanistic insights into an archaeal DNA-guided Argonaute protein. *Nat Microbiol* **2**, 17035 (2017).
38. Doxzen KW, Doudna JA. DNA recognition by an RNA-guided bacterial Argonaute. *PLoS One* **12**, e0177097 (2017).
39. Wang X, *et al.* Structural insights into mechanisms of Argonaute protein-associated NADase activation in bacterial immunity. *Cell Res* **33**, 699-711 (2023).
40. Ni D, Lu X, Stahlberg H, Ekundayo B. Activation mechanism of a short argonaute-TIR prokaryotic immune system. *Sci Adv* **9**, eadh9002 (2023).
41. Shen Z, *et al.* Oligomerization-mediated activation of a short prokaryotic Argonaute. *Nature* **621**, 154-161 (2023).
42. Jurgelaitis E, *et al.* Activation of the SPARDA defense system by filament assembly using a beta-relay signaling mechanism widespread in prokaryotic Argonautes. *Cell Res* **35**, 1056-1078 (2025).
43. Kanevskaya A, *et al.* Argonaute-HNH filaments triggered by invader DNA confer bacterial immunity. *Nat Commun* **16**, 11389 (2025).
44. Wang F, Xu H, Zhang C, Xue J, Li Z. Target DNA-induced filament formation and nuclease activation of SPARDA complex. *Cell Res* **35**, 510-519 (2025).
45. Abramson J, *et al.* Accurate structure prediction of biomolecular interactions with AlphaFold 3. *Nature* **630**, 493-500 (2024).
46. Cui N, Zhang JT, Li Z, Wei XY, Wang J, Jia N. Tetramerization-dependent activation of the Sir2-associated short prokaryotic Argonaute immune system. *Nat Commun* **15**, 8610 (2024).
47. Yang XY, Shen Z, Wang C, Nakanishi K, Fu TM. DdmDE eliminates plasmid invasion by DNA-guided DNA targeting. *Cell* **187**, 5253-5266 e5216 (2024).
48. Loeff L, *et al.* Molecular mechanism of plasmid elimination by the DdmDE defense system. *Science* **385**, 188-194 (2024).

49. Thompson RF, Iadanza MG, Hesketh EL, Rawson S, Ranson NA. Collection, pre-processing and on-the-fly analysis of data for high-resolution, single-particle cryo-electron microscopy. *Nat Protoc* **14**, 100-118 (2019).
50. Zivanov J*, et al.* New tools for automated high-resolution cryo-EM structure determination in RELION-3. *Elife* **7**, (2018).
51. Zheng SQ, Palovcak E, Armache JP, Verba KA, Cheng Y, Agard DA. MotionCor2: anisotropic correction of beam-induced motion for improved cryo-electron microscopy. *Nat Methods* **14**, 331-332 (2017).
52. Zhang K. Gctf: Real-time CTF determination and correction. *J Struct Biol* **193**, 1-12 (2016).
53. Punjani A, Rubinstein JL, Fleet DJ, Brubaker MA. cryoSPARC: algorithms for rapid unsupervised cryo-EM structure determination. *Nat Methods* **14**, 290-296 (2017).
54. Jumper J*, et al.* Highly accurate protein structure prediction with AlphaFold. *Nature* **596**, 583-589 (2021).
55. Emsley P, Lohkamp B, Scott WG, Cowtan K. Features and development of Coot. *Acta Crystallogr D Biol Crystallogr* **66**, 486-501 (2010).
56. Liebschner D*, et al.* Macromolecular structure determination using X-rays, neutrons and electrons: recent developments in Phenix. *Acta Crystallogr D Struct Biol* **75**, 861-877 (2019).

Acknowledgements

We thank the staff members from Cryo-Electron Microscopy Facility of Hubei University for help on data collection and computation. We thank the reviewers for the thoughtful comments and detailed suggestions on the paper. This work was supported by China National Key Research and Development (R&D) Program (2023YFA0913700); Project of Technological Innovation Plan in Hubei Province (2024BCA001); the China Postdoctoral Science Foundation (2023M741100); the Basic Research Platform Project of Science and Technology Program Project in Hubei Province (2025CSA129); the Natural Science Foundation of Wuhan City (2024040701010046); and Major Special Project for the Development of the Agricultural Microbiology Industry in Hubei Province (NYWSWZX2025-2027-10).

Author contributions

L.M., Z.L. and W.L. supervised the study. W.L., Y.H., F.L., and J.Z. prepared the samples. C.Z. and Z.L. collected and processed the cryo-EM data and built the atomic model. W.L., Y.H., F.L., and J.Z. performed the biochemical analysis. W.L. prepared the manuscript and figures with input from L.M., and Z.L. All authors analyzed the data.

Competing interests

The authors declare no competing interests.

Figure Legends

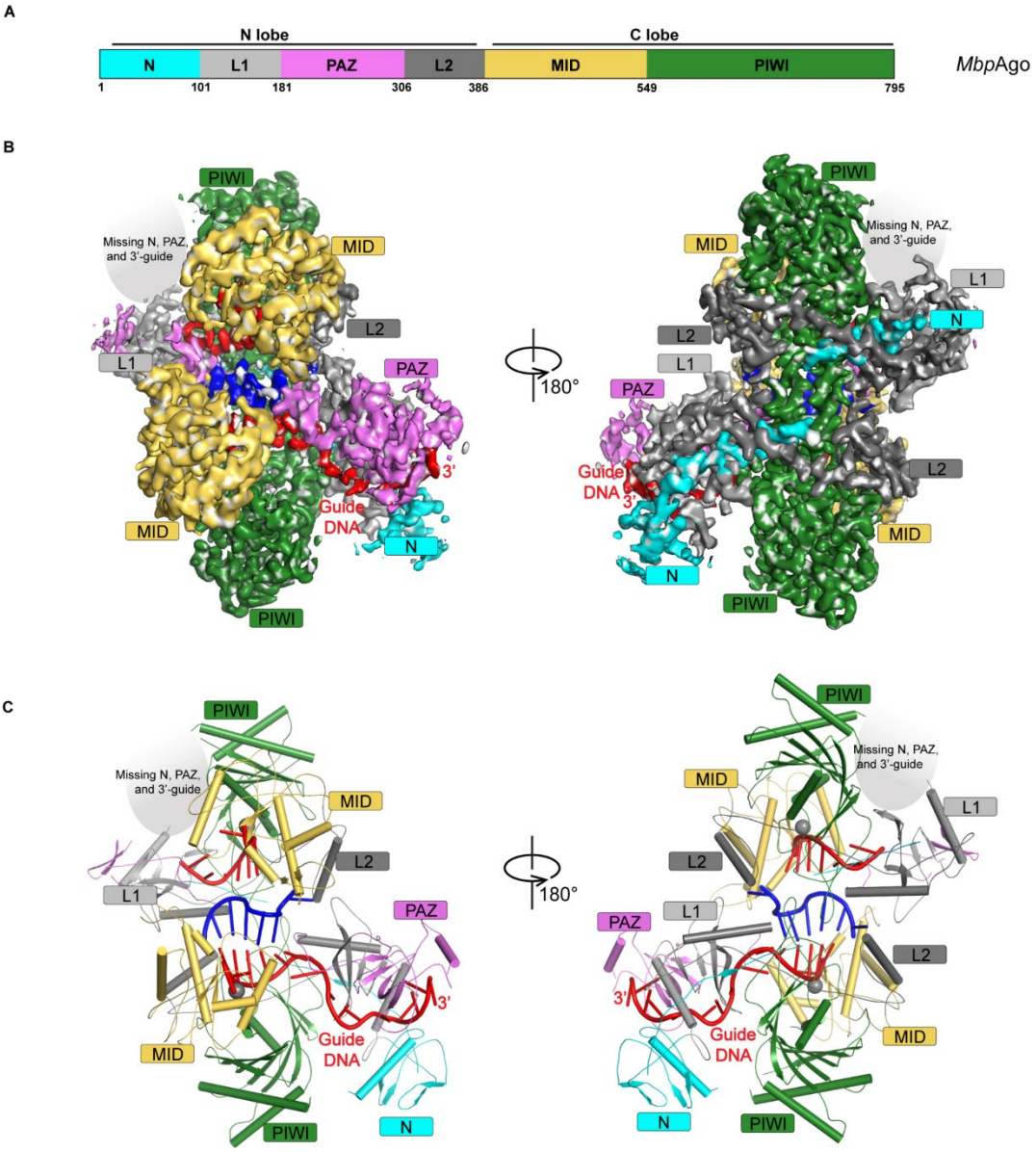


Figure 1. Structure of MbpAgo-guide DNA binary complex. (A) Domain Architecture of MbpAgo. **(B, C)** Overall structure of MbpAgo-guide DNA binary complex in two different views. Protein domains are colored as in panel A. The Mg^{2+} ion is shown in gray, the guide DNA in red, and the excess DNA density (putative candidate target DNA) in blue.

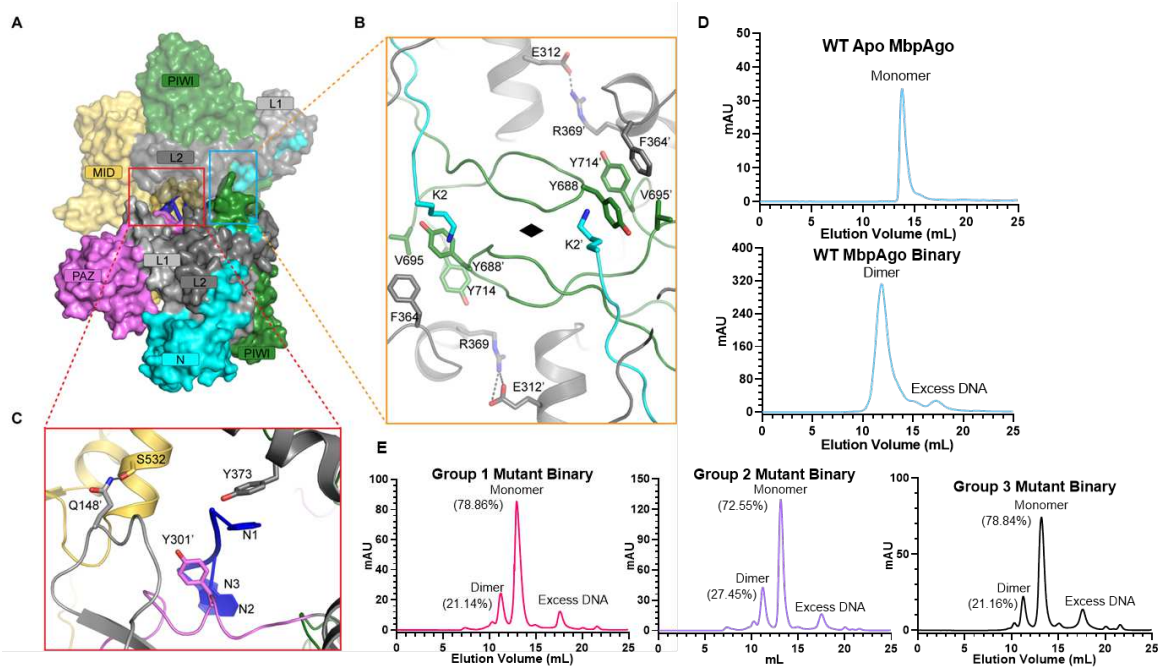


Figure 2. Dimerization of MbpAgo. (A) Surface representation of MbpAgo-guide DNA binary complex. The rectangles with different colors represent different dimerization interfaces. **(B)** Interaction details at PIWI-PIWI and L2-L2 interface. **(C)** Interaction details between terminal nucleotides (the excess nucleic acid) and L2 and PAZ domains. **(D)** Size exclusion chromatography (SEC) of Apo-MbpAgo and wild-type MbpAgo-gDNA complex. **(E)** SEC of the mutant MbpAgo-gDNA complexes (Group 1, Group 2 and Group 3). Group 1 mutation includes Y301A, Y373A, and R530A. Group 2 mutation includes R369A, E312A, Y688A, F364A, V695A, Y714A, and K2A. Group 3 mutation K684-Q690 with two Gly. The three peaks of the elution profile indicate dimer, monomer, and excess DNA, respectively. The dimer/monomer ratios were calculated based on the area of the respective peaks.

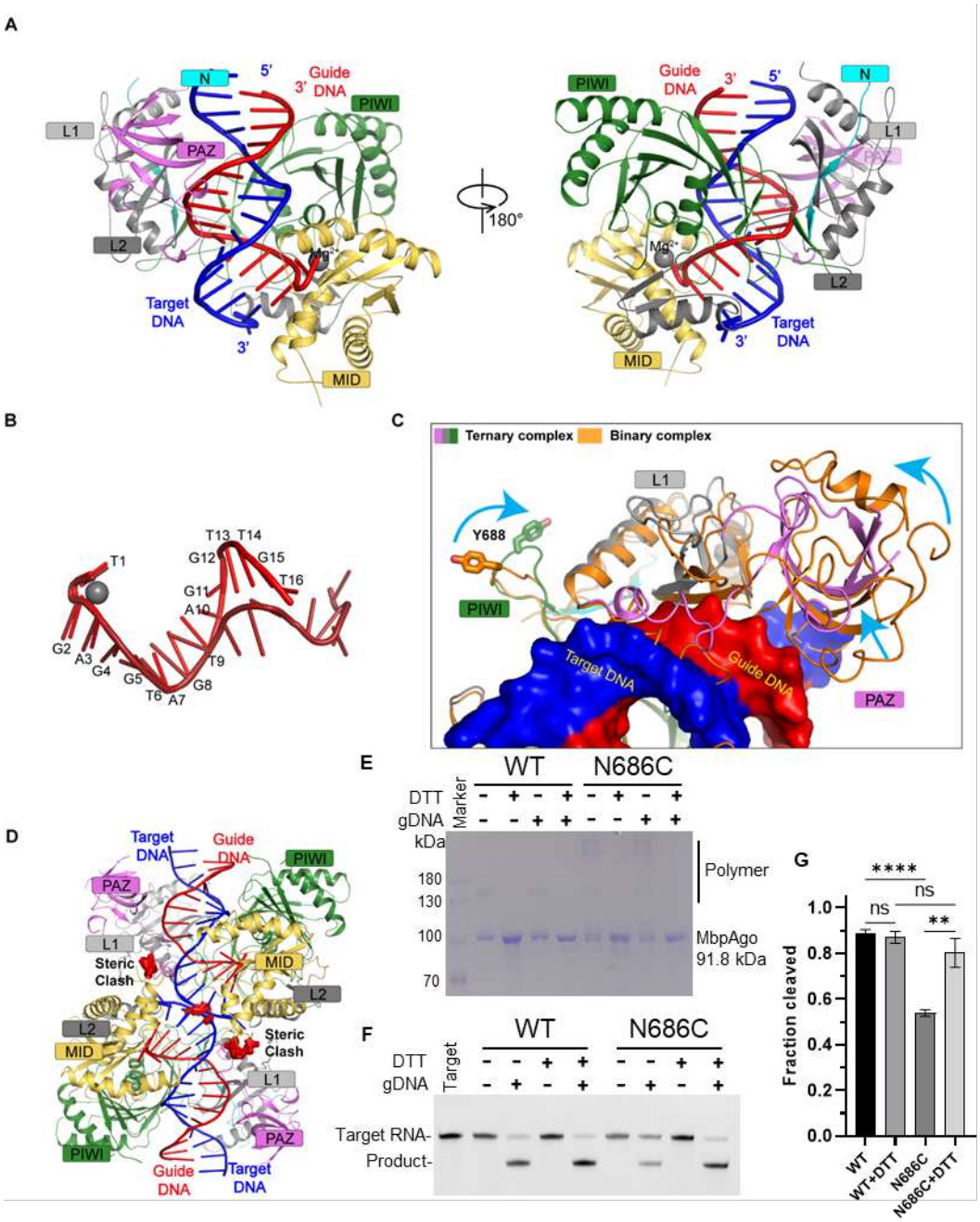


Figure 3. Structure of MbpAgo-guide DNA-target DNA ternary complex. (A) Overall structure of MbpAgo-gDNA-target DNA ternary complex in two different views. Domains are colored as in Figure 1A. Mg^{2+} is shown in gray, guide DNA in red, and target DNA in blue. **(B)** Superposition of gDNA in the binary complex and ternary complex. **(C)** Conformational differences between the dimeric (binary) and monomeric (ternary) states, highlighting rearrangement of the PAZ domain and inversion of the PIWI loop (residues 684–690). **(D)** Superposition of two copies of the ternary complex onto the dimeric binary complex reveals steric clashes. Residues and nucleotides involved in clashes are shown as sticks. **(E)** Polymerization of the N686C mutant at the PIWI-PIWI interface in MbpAgo-gDNA complex **(F)** Target RNA cleavage assays comparing wild-type MbpAgo and the N686C mutant in the presence or absence of 5 mM DTT. **(G)** Quantification of cleavage efficiency. Data are representative of three independent experiments.

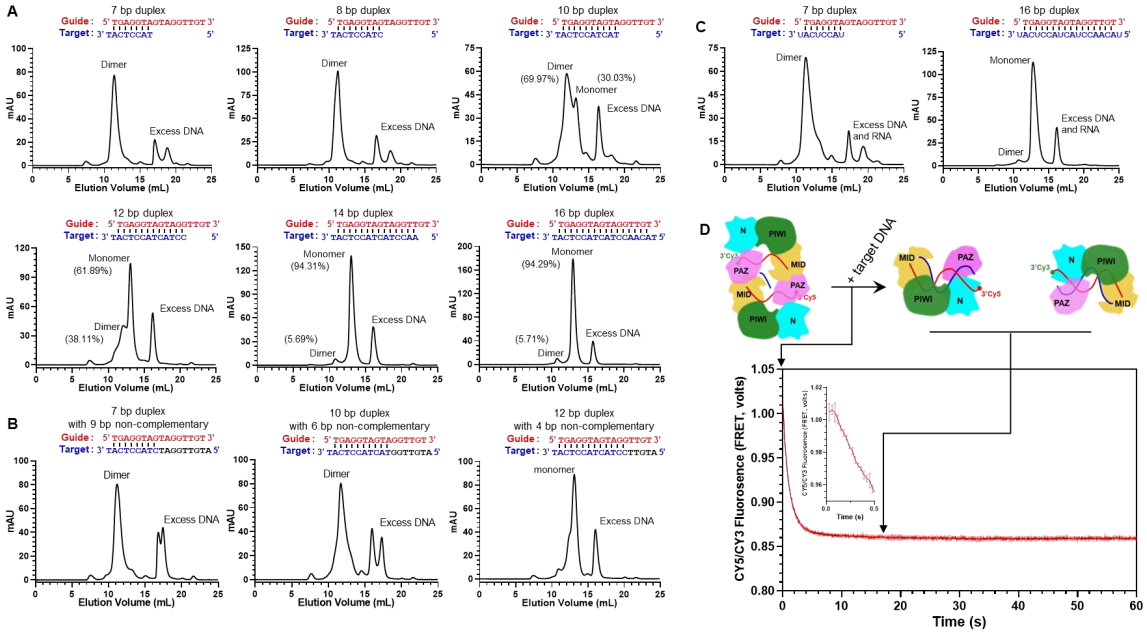


Figure 4. Target-induced dimer-to-monomer transition of MbpAgo. (A) SEC analysis of ternary complexes formed by MbpAgo with a 16-nt guide DNA and target DNAs of varying lengths. **(B)** SEC analysis of ternary complexes formed by MbpAgo with a 16-nt guide DNA with fully or partially matched 18-nt target DNAs. **(C)** SEC analysis of ternary complexes formed by MbpAgo with a 16-nt guide DNA and target RNAs of varying lengths. **(D)** Stopped flow fluorescence measurements of target binding were monitored by FRET-induced decrease of Cy5/Cy3 fluorescence. FRET experiment to measure the dimer dissociation upon adding target DNA.

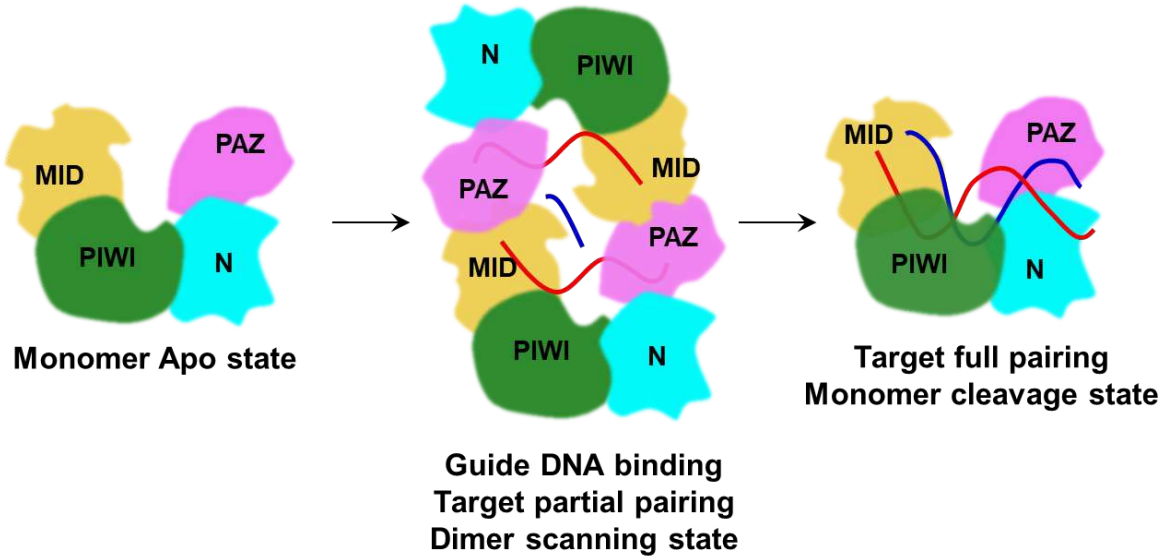


Figure 5. A proposed working model for the dimerization and activation of MbpAgo.
Guide DNA is colored in red, target DNA is colored in blue, and the protein is colored based on Figure 1A. The cartoons of the binary complex and ternary complex are drawn in the same view angle as Figure 1B and 3A. Apo MbpAgo exists predominantly as a monomer. Upon guide loading and candidate target sampling via seed pairing, MbpAgo forms a scanning-competent dimer. Extension of guide–target base pairing beyond ~12 bp destabilizes the dimer interface, triggering de-dimerization and formation of a catalytically competent monomer.

535 **Table 1. Cryo-EM data collection, refinement and validation statistics**

536

	MbpAgo-guide DNA (PDB: 22UE, EMD-68672)	MbpAgo-guide DNA-target DNA (PDB: 22UF, EMD-68673)
Data collection and processing		
Magnification	105,000	105,000
Voltage (kV)	300	300
Electron exposure (e^{-}/Å^2)	54	54
Defocus range (-μm)	1.2 – 2.2	1.2 – 2.2
Pixel size (Å)	0.85	0.85
Symmetry imposed	*C1*	*C1*
Initial particle images (no.)	2,034,645	4,017,853
Final particle images (no.)	274,970	964,147
Map resolution (Å)	3.2	3.1
FSC threshold	0.143	0.143
Map resolution range (Å)	3.0 – 4.2	3.0 – 3.8
Refinement		
Initial model used	AlphaFold2	AlphaFold2
Model resolution (Å)	3.2	3.4
FSC threshold	0.5	0.5
Model resolution range (Å)	3.0 – 4.2	3.0 – 3.8
Map sharpening *B* factor (Å^2)	–90	-100
Model composition		
Non-hydrogen atoms	11418	5635
Protein residues	1314	610
Nucleotides	31	31
B factors (Å^2)		
Protein	88.82	56.93
Nucleotide	50.99	68.49
R.m.s. deviations		

Bond lengths (Å)	0.004	0.004
Bond angles (°)	0.978	0.978
Validation		
MolProbity score	1.92	1.73
Clashscore	7.28	6.53
Poor rotamers (%)	0.93	0.18
Ramachandran plot		
Favored (%)	90.96	94.63
Allowed (%)	9.04	5.37
Disallowed (%)	0.00	0.00

537

Supplementary Files

This is a list of supplementary files associated with this preprint. Click to download.

- NatureCommunicationsMbpAgoSI.pdf
- D1300069160valreportfullannotateP1.pdf
- D1300069121valreportfullannotateP1.pdf
- nrreportingsummary.pdf